JOM Journal of Optical Microsystems

RESEARCH PAPER

Engineered scattering elements used as optical test points in photonic integrated circuits

Tyler V. Howard,* Icel Sukovaty, and Thomas G. Brown
University of Rochester, The Institute of Optics, Rochester, New York, United States

ABSTRACT. Efficient packaging of fabricated photonic integrated circuits (PICs) has been a daunting task given the breadth of applications and skill required for scalable manufacturing. One particular challenge has been accurately assessing the polarization state at various points in a PIC during the test, assembly, and packaging process. Polarimetric monitoring is necessary for optimizing fiber alignment, for verifying the quality of PIC components and for polarization-related functional testing. We analyze and demonstrate small-footprint engineered scattering elements for polarization monitoring. We find that small scatterers placed above or below a Si or SiN waveguide provide the best polarization integrity in a way that preserves foundry compatibility. The polarization response of these elements along with proper placement provides an optical test point that can be utilized for optimized fiber coupling into waveguides.

© The Authors. Published by SPIE under a Creative Commons Attribution 4.0 International License. Distribution or reproduction of this work in whole or in part requires full attribution of the original publication, including its DOI. [DOI: 10.1117/1.JOM.4.1.011002]

Keywords: photonics; scattering; polarization; finite-difference time-domain; coupling

Paper 23012SS received Jun. 14, 2023; revised Aug. 28, 2023; accepted Aug. 31, 2023; published Nov. 23, 2023.

1 Introduction

Photonic integrated circuits (PIC) fabricated on a silicon on insulator (SOI) platform have become the basis for expanding technologies that continue to demand higher performance. Applications of PICs have grown to include optical communications,[1–4] biomedical optics,[5] sensing,[6–8] electro-optic interconnects,[9–11] and quantum technologies.[12,13] The SOI fabrication platform is the most widely used and accepted standard across the photonic/semiconductor industry. However, emerging businesses/technologies may not have access to the equipment necessary to successfully fabricate these PICs. National foundries, such as the AIM Photonics Foundry, have begun to be established, which allows for more access to PIC technology/design, with improvement and testing of their processes an ongoing process and active area of research to the industry community.

While the SOI platform is desirable because of its compatibility with CMOS devices,[4,7] packaging of completed devices is still a difficult hurdle to clear for PICs to become a widely accepted commodity. Two challenges that are routinely investigated and improved are optical source coupling[14] and electrical connections.[15] The challenges with electrical connects will not be addressed in this article; we will instead focus on the optical aspect of PIC test, assembly, and packaging. Coupling an optical source to a PIC is typically achieved through: (a) an optical fiber that is edge coupled along a facet edge or grating coupled through the surface[14,16] or (b) integrated laser sources that are flip-chip bonded to the surface.[17,18] Light from optical fibers is sensitive to misalignment, where displacement by a few microns can result in a significant reduction of

*Address all correspondence to Tyler V. Howard, thoward9@ur.rochester.edu

optical power coupled to the waveguide. Utilizing V-grooves[19] or slots along the PIC edge helps in alignment, especially with fiber arrays, but these only provide a passive tool toward alignment but cannot securely hold the fibers in place.

Testing of completed PIC designs involves characterizing the fiber alignment, waveguide loss, optical performance, and electrical responsivity. Fiber alignment is especially crucial for efficient circuit operation; multiple methods have been demonstrated to help with passive alignment. When attached using epoxy, the fiber can shift as the epoxy cures. The results of this process are challenging to correct; some recent work has demonstrated a new fusion technique to bond fibers to a PIC.[20] Guided modes coupled from the optical fiber interact with components placed down stream. Currently, no standardized method exists for evaluating individual component performance.[21] In addition, testing of the waveguide losses is characterized with taps and integrated power detectors. For external inspection, a short-wave infrared (SWIR) microscope setup can be employed to determine whether a component has higher than expected losses, but typically cannot quantify or localize the losses.

A key problem thus far neglected is the monitoring of the polarization of light at various points in a circuit; this is especially important in optical communications for multiplexing signals in a waveguide.[22] The large birefringence of the SOI platform requires the need for very pure polarization states to be emitted from the coupled optical source to achieve very large signal-to-noise ratios.[23] Most established foundries have components in their process-design-kits work on the fundamental TE/TM modes. Achieving either of these modes independently is no easy task with polarization management techniques being developed to convert or attenuate any light of an undesired polarization state.[23–29] While these techniques are functional, implementation requires additional photodetectors or spots for output fiber couplers to be included in the PIC design, thus taking away valuable PIC real estate that could be used to experiment with alternative designs.

It has long been known, and usefully applied, that a microscope-camera setup can capture scattered light to track signal paths in a PIC.[30] However, the stochastic nature of the scattering process lends little information useful for quantitative diagnostics. Grating couplers, tap/detector combinations, and near field probes have been used as a means of sampling guided light but typically require a significant amount of chip real estate.[31,32] Near field probes cannot adequately sample the field in foundry completed PICs where the upper cladding has a thickness $>1\ \mu$m.[33,34] Lombardo et al.[35] demonstrated the use of designed scattering as optical test points for loss measurements but requires a two-step process of annealing and subsequent removal before completing the chip. Thus, there is a significant need for foundry-compatible optical test points that provide a faithful and consistent probe of the guided power and/or polarization state of the light without sacrificing chip real estate.

In this paper, we present the design, polarization response, and fiber alignment monitoring technique for several classes of engineered scatterers. The polarization responses of the scattering elements were evaluated for the fundamental TE and TM modes using an SWIR microscope and are compared with numerical simulations. Treating the scattering elements as optical test points, we monitored the relative scattered power as a fiber was raster scanned along the facet edge. In the following sections, we describe the design, fabrication, modeling, and experimental testing of these features.

2 Scattering Element Design and Fabrication

The scattering elements were designed using finite element modeling in Ansys-Lumerical's software platform. The primary design constraints were structured to be consistent with layer thicknesses of PICs fabricated through the AIM Photonics foundry process.[36] This process has two waveguide material selections: silicon (Si) and silicon-nitride (SiN) with nominal widths/heights of 480/220 and 1200/220 nm, respectively, with single mode operation for typical operating wavelengths of 1550 and 1300 nm. Waveguides in all cases are surrounded by a SiO_2 cladding. Through the AIM Photonics foundry, there are three available waveguides layers: a silicon layer, first nitride (FN) layer, and second nitride (SN) layer. A diagram of the waveguides is shown in Fig. 1(a).

Acquiring quantitative data from the scattering element requires that a readily detectable amount of light from the scatterers reach the camera while maintaining low overall loss and

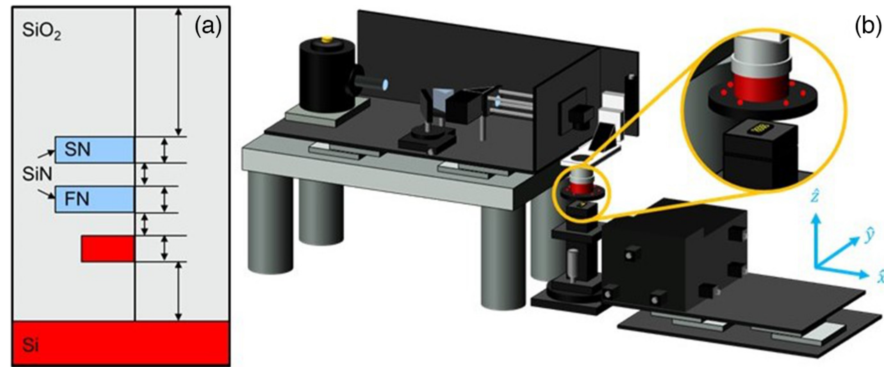

Fig. 1 (a) Schematic of waveguide layers in foundry process and (b) SWIR microscope used for analysis with coordinate system. Double-ended arrows in (a) represent a preset thickness that is dependent on each foundry.

minimizing back-scatter into the waveguide. An initial starting point for this was to design a scattering element with subwavelength lateral dimensions (200 nm × 200 nm) and a thickness equal to that of a standard waveguide placed adjacent to the waveguide on the same material layer. The initial width and length dimensions were chosen based on the Foundry's design rules which limited the smallest feature size on the silicon layer to 200 nm. Future designs incorporated the FN and SN layers of the AIM platform while this paper focuses on designs using the FN layer. Using geometries of this size allows for the source to be approximated as a dipole source whose polarization axis is parallel to the polarization state of the local electromagnetic field.

3 Numerical Modeling

To better understand scattering effects from engineered elements, scatterers were numerically simulated by combining a finite-difference time-domain (FDTD) waveguide analysis with vector-field propagation through the microscope objective to the pupil plane. Further propagation of the computed electric fields was performed through Fourier propagation integrals.[37] We describe the FDTD and vector-propagation models below.

3.1 Finite-Difference Time-Domain

Subwavelength scattering elements were first modeled using FDTD methods to provide the most accurate and holistic picture of scattered electric fields. Using the Ansys-Lumerical FDTD solver engine, initially three different scattering element configurations were simulated. Each configuration is based on the material of the scattering element and waveguide, where each configuration will be referred to as follows: silicon scatterer–silicon waveguide (Si-Si); silicon-nitride scatterer–silicon waveguide (SiN-Si); and silicon scatterer–silicon-nitride waveguide (Si-SiN). Each scattering configuration was constructed in a three-dimensional (3D) CAD environment with physically accurate spacing found in the AIM wafers. The input fields were defined to match the ideal TE and TM modes of the waveguides; however, since SOI is an inherently leaky-mode platform, mode matching is never numerically perfect. It was therefore necessary to propagate the guided light around a waveguide bend before encountering the scatterer in order to minimize the interaction of unguided light with the scatterer. A visual example of the input mode profiles along with their response with a scatterer beside/above the waveguide is provided in Fig. 2. It was also important to carefully compare the calculated background fields (those present without the scatterer) with those fields with the scatterer present to properly isolate the scattered fields. Monitors in FDTD simulations were placed before and after the scattering element in the waveguide to evaluate power scattered by the element, with a large monitor above the element in the z-direction to capture scattered fields upwards toward the camera.

3.2 Numerical Vector-Field Propagation

Near-fields computed from Ansys-Lumerical's FDTD solver were numerically propagated to the microscope pupil plane (far-field) accounting for material interfaces and 3D coordinate

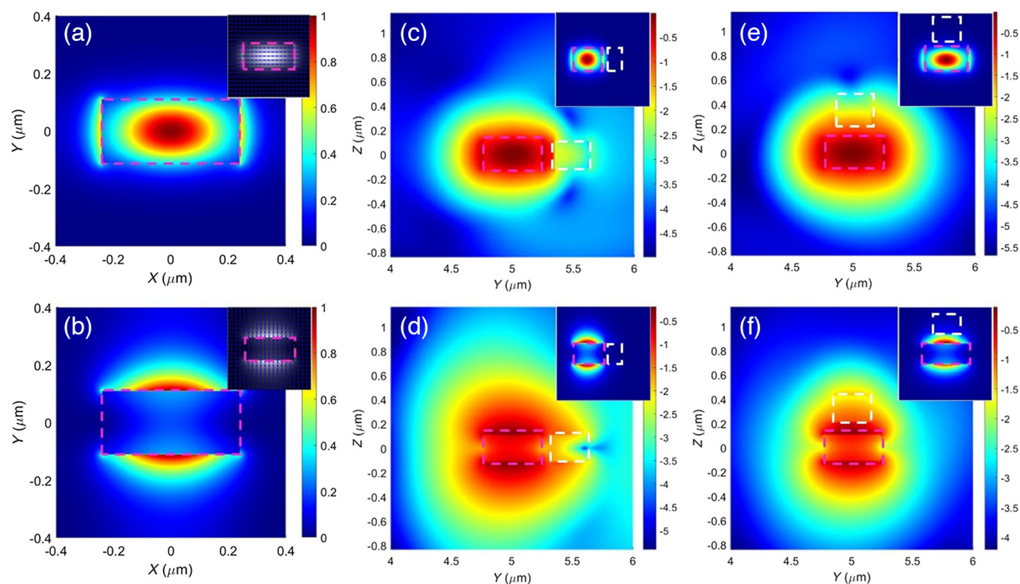

Fig. 2 Mode profiles of electric fields in FDTD simulations. Input mode profiles for (a) TE and (b) TM with insets showing the polarization observed along the propagation axis. Mode profiles on a log-base 10 scale of inputs interacting with scattering element beside the waveguide for (c) TE and (d) TM. Profiles when the scatterer is above the waveguide for (e) TE and (f) TM inputs: also on a log-base 10 scale. Insets of (c)–(e) are on a linear scale. Waveguides are outlined with a pink dashed rectangle and scatterers a dashed white rectangle.

transformations from microscope focusing. Electric fields generated from engineered scattering elements possessed a non-negligible component parallel to the direction of propagation, that is reduced to zero in the pupil plane upon focusing through the microscope objective. For the scattering elements, we define the z-axis as the propagation direction. (Visual reference for the coordinate system is provided in Fig. 3.) In addition to the transformation of the z-component, fields in the pupil must account for the refraction and polarization-dependent transmission through the intermediate SiO_2–air interface. Computations for generating these fields are broken down into three segments: (I) angular spectrum of fields in SiO_2, (II) fields in the air-space between the PIC cladding and the microscope objective, and (III) collimated fields in the pupil plane. Subscripts of the total electric field (e.g., I) correspond to the region where fields lie.

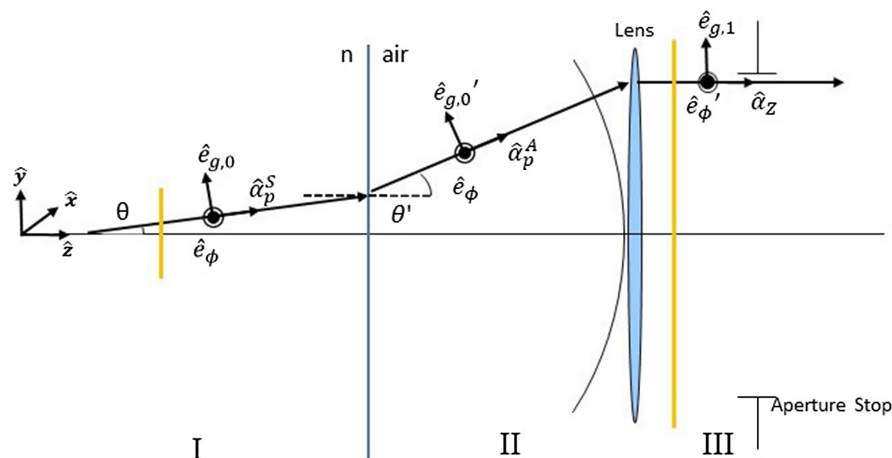

Fig. 3 Diagram displaying vector transforms utilized for calculation of fields in the pupil plane of a microscope. Diagram is broken into three regions with the following fields: (I) Fourier transform of near fields from FDTD simulation while in the SiO_2, (II) fields after refraction and polarization-dependent transmission, and (III) final pupil fields after adiabatic vector transform.

For every scattering element simulated, the light scattered from these elements propagates into the upper half-space above with a portion collected by a microscope objective. The fields collected by the objective map to the angular spectrum of the input and are observable at the back focal plane of the objective. Thus, given the physical specifications of the microscope system, the Fourier transform of each near field component can be computed using direction vectors having an origin at the scatterer.[37,38] Based on the direction vectors computed in the Fourier transform, each field component was separated into tangential (denoted as $\hat{e}_{\phi}$, $\hat{e}_{g,0}$) and propagating field contributions (expressed as $\hat{\alpha}_p^S$). The unit vectors $\hat{e}_{\phi}$ and $\hat{e}_{g,0}$ are the azimuthal and orthogonal tangential vector, respectively. From this, the angular spectrum of the electric fields from the near field in the SiO_2 can be expressed as

$$\vec{\mathbf{E}}_{\mathbf{I}}^{\mathbf{f}} = E_{\phi}^{f}\hat{e}_{\phi} + E_{g,0}^{f}\hat{e}_{g,0}, \tag{1}$$

where $\vec{\mathbf{E}}^{\mathbf{f}}$ denotes the Fourier transform of the electric field from FDTD computations. Transmission/refraction through the SiO_2–air interface requires knowledge of the angle of incidence for each propagation direction; these are defined by the direction vectors of the Fourier transforms and allow a straightforward computation of both the polarization dependent transmission and the coordinate shift arising from refraction. The angular spectrum calculated from a Fourier transform of the near fields is then multiplied by these transmission coefficients and component values shifted per refraction. Accounting for refraction and transmission from the material interface, electric fields can then be expressed as

$$\vec{\mathbf{E}}_{\mathbf{II}}^{\mathbf{f}} = t_s E_{\phi}^{f}\hat{e}_{\phi} + t_p E_{g,0}^{f}\hat{e}'_{g,0}, \tag{2}$$

where $t_{s,p}$ are the transmission coefficients and the prime denotes the change in angle from SiO_2 to air. Note that the meridional component $\hat{e}_{\phi}$ does not change upon refraction since this component is parallel to the interface. Electric fields focused through an optical element undergo a vector transform from the acquired quadratic phase, thus an adiabatic vector transform method was employed to compute the final fields. This type of adiabatic transformation has already been documented by Richards and Wolf in 1959.[39] Upon applying this vector transformation, the fields in the pupil are

$$\vec{\mathbf{E}}_{\mathbf{III}}^{\mathbf{f}} = t_s E_{\phi}^{f'}\hat{e}_{\phi} + t_p E_{g,1}^{f}\hat{e}_{g,1}, \tag{3}$$

where the new field components are $E_{g,1}^{f}$, and $\hat{e}_{g,1}$ is the new orthogonal tangential field component. A visual diagram of this propagation, with vector coordinate basis, is shown in Fig. 3. Further propagation and polarization analysis of the calculated fields becomes a more trivial task, as the z-component of the electric fields are now zero and standard computational techniques (e.g., Fresnel diffraction using Fourier transforms) can be employed.[37]

The numerical calculation was tested using an idealized Rayleigh scatterer (i.e., sphere with diameter $<\lambda/10$) introduced into the center of the waveguide. Such a scatterer is expected to produce an ideal dipole field, with the polarization of the dipole aligned with the polarization state of the waveguide mode at the location of the scatterer. Thus, in our laboratory frame, a TE polarized mode will radiate as a transverse dipole, while a TM polarization will, theoretically, produce a z-dipole orientated along the optical axis of the microscope objective. Calculated FDTD fields displayed the expected radiation pattern of an electric dipole with the dipole axis aligned with the waveguide polarization. Numerical propagation then allows a polarization analysis of the scattered fields evaluated at the pupil plane of the microscope. Since the polarization of light from an electric dipole is dependent on the orientation of the optical axis with respect to the dipole axis,[40] a dipole oriented orthogonal to the optical axis produces a purely linear polarization state in the pupil, while a dipole oriented parallel to the optical axis produces a spatially varying (radial) polarization state.[41] Polarization maps (shown in Fig. 4) of the Rayleigh scatterer matched expected results, with a TE mode yielding a linear state and a TM mode yielding a radial state with the major axis rotating about the center, shown in Fig. 4(d).

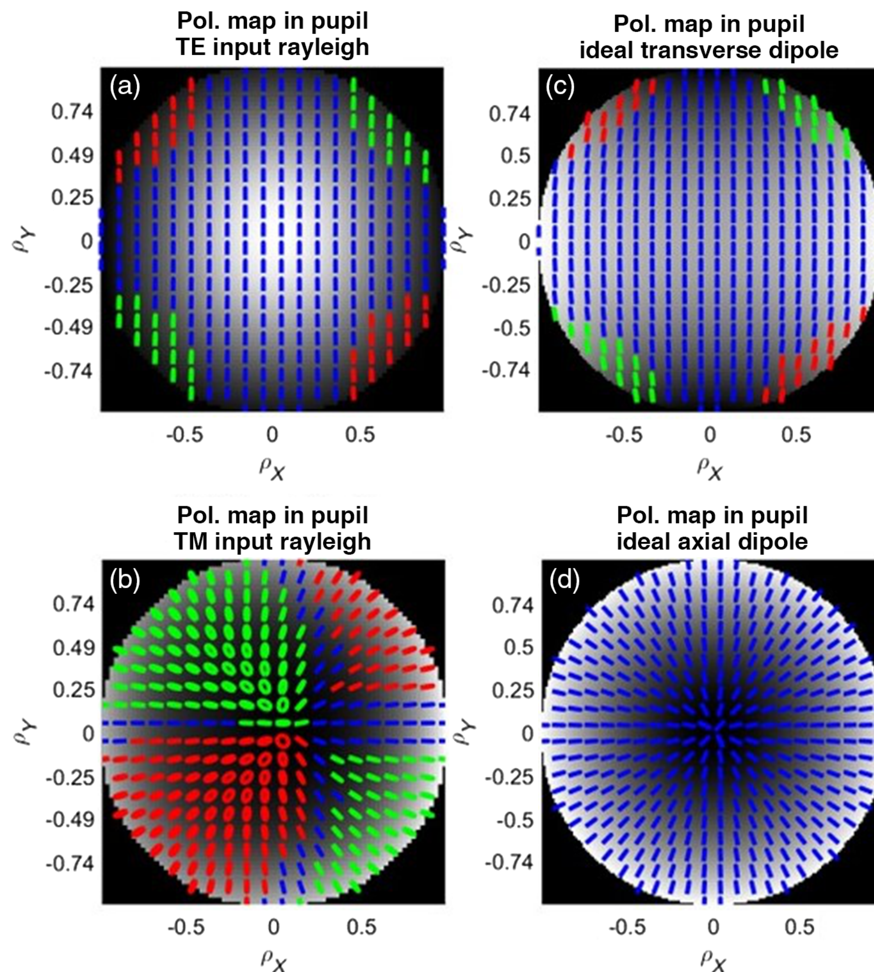

Fig. 4 Polarization ellipses plotted within the pupil plane of simulations placing a Rayleigh scattering element in the waveguide for (a) TE and (b) TM inputs. Results of an ideal dipole scattering element are shown for (c) a transverse vertical dipole and (d) an axial dipole. Polarization states are color coded as linear-blue, left-hand elliptical (LHE)-green, and right-hand elliptical (RHE)-red.

4 Experimental Observation

4.1 Experimental Setup and Scattering Signal

Light scattered from an engineered scattering element was collected and imaged using the custom-built SWIR microscopy system shown in Fig. 1(b). Fabricated PICs were imaged under a dark-field illumination setup for PIC/fiber alignment. Light from a cleaved fiber was edge coupled into the PIC through a six-axis positioning system (Thorlabs, Newton, New Jersey) for optimal alignment and polarization input. Scattered light from the engineered scattering elements was captured with a 0.4 NA infinity-corrected microscope objective (Mitutoyo: Sakado, Japan), imaged to an indium-gallium-arsenide CCD sensor (Princeton Instruments: Trenton, New Jersey). Pixel saturation of the CCD camera occurred at $\sim 42,000$ counts across all images. Input light levels were attenuated such that the maximum pixel response of any scattering element was below this threshold during data capture.

Images of engineered scattering elements captured under the SWIR microscope display an easily distinguishable signal that is at least an order of magnitude greater than the background scattering from the PIC. Observation of PICs under dark-field illumination shows no presence of engineered scattering elements by the waveguides with system resolution diffraction limited to $\approx 4.7\ \mu$m. When light from a cleaved fiber is edge coupled into the necessary waveguide, the scattering element can readily be observed even with the competing dark-field illumination. Images of engineered scattering elements are shown in Fig. 5.

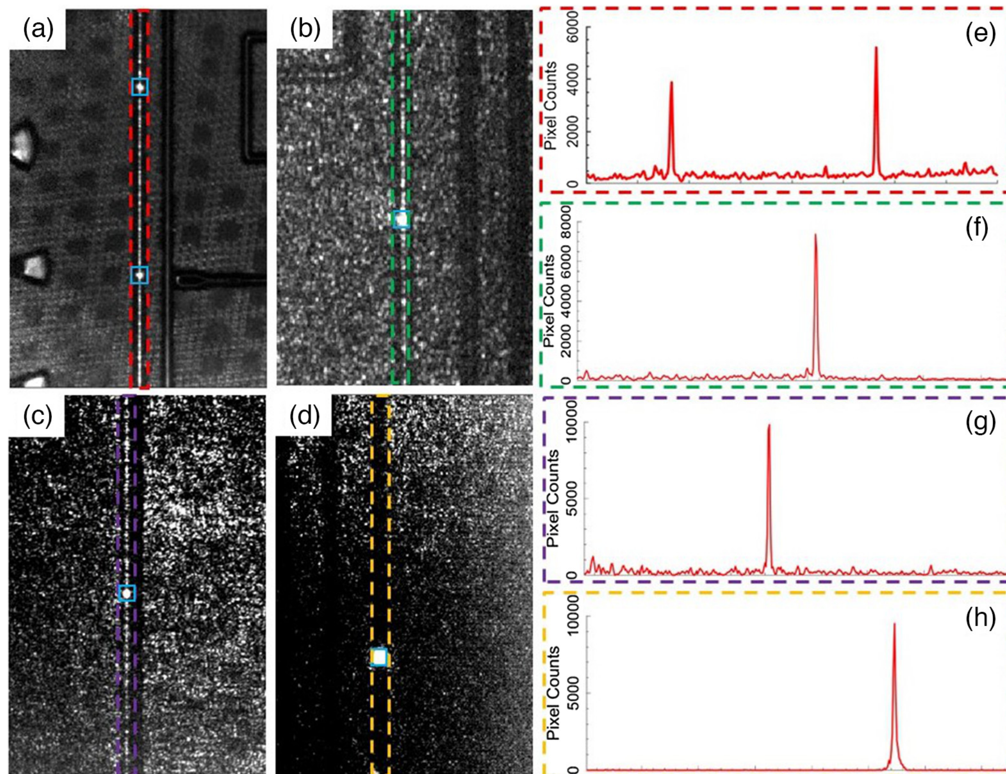

Fig. 5 Engineered scattering elements in PICs captured with an SWIR microscopy system, with line-outs of pixel counts along accompanying waveguide. Configurations of scattering elements and waveguides are given as (a) Si-Si: 1 μm separation, (b) Si-Si: 100 nm separation, (c) SiN-Si, and (d) Si-SiN. Engineered scattering elements are outlined in a blue box with line-outs for each scattering element configuration provided to the right of each image, with the colored box outlining the region of interest for each line-out. Line-outs for each image are (e) corresponds to (a), (f) to (b), (g) to (c), and (h) to (d).

The signal from each scattering element is clearly distinguishable for each scattering element even with large coupling distances from the waveguide to the scattering element. The material for the waveguide can vary based on the desired application of the user; each configuration of scattering elements listed in Sec. 2 was therefore tested. We first consider a scattering element within the silicon layer and adjacent to the waveguide layer but designed with identical thickness (the Si-Si design). A scattering element spaced 1 μm from the waveguide provided a contrast of 11.4× with the background scattering of the waveguide. An example of scattering elements in this configuration is shown in Fig. 5(a). Moving the scattering element closer to the waveguide (to within 100 nm of separation) allowed the element to scatter more light from the waveguide, producing a contrast of 53.1× in the most recent fabrication runs. An image of this scattering element is shown in Fig. 5(b). Utilizing the adjacent material layers allows for increased design options in the PIC, allowing for scattering element—waveguide configurations, such as SiN-Si and Si-SiN. Contrast from these configurations displayed similar results with the previous two iterations. Contrasts for the SiN-Si and Si-SiN configurations were evaluated to 50.0× and 4020×, respectively.

4.2 Observed Polarization Response

Scattering elements were then tested to determine their polarization response, with two configurations (SiN-Si and Si-SiN) displaying strongly correlated polarization states with the input modes. The main figure of merit to quantify a scattering elements polarization response is the extinction ratio defined as $P_{||}/P_{\perp}$, where $P_{||,\perp}$ is the power when the analyzer is parallel and perpendicular to the input polarization state, respectively. Using birefringent fiber paddles,

Table 1 Summary of extinction values captured from fabricated engineered scattering elements with noise from the standard deviation across all trials.

Scattering conf. (fiber)	TE extinction	TM extinction
Si-Si	1.38 ± 0.121	5.87 ± 2.52
SiN-Si	73.8 ± 45.6	62.4 ± 33.0
Si-SiN	146 ± 97.1	2.71 ± 0.827

TE/TM (horizontal/vertical) light was coupled into a waveguide with a linear analyzer placed before the tube lens for extinction of orthogonal polarization states. Images captured of the analyzer in parallel and perpendicular orientations with the input light allow for calculation of the extinction ratio of each scattering element. For the Si-Si designs, the pupil polarization was not strongly correlated with the input modes. Inputting a TE mode into the PIC and rotating the polarizer 90 deg displayed little extinction from the scattering elements, when comparing a vertical analyzer to a horizontal analyzer: extinction values for TE modes were calculated to be ~ 1.4. Moving the scattering element directly above the silicon waveguide in the FN layer showed a more favorable polarization discrepancy between orthogonal states. Analysis of captured images showed a TE extinction ~ 74 between the orthogonal linear states. Going to the Si-SiN configuration yielded even greater results, with extinction ratios reaching on average 146 for TE modes. A full summary of the extinction values for all input modes is provided in Table 1.

4.3 Fiber Optic Edge Coupling

It is possible to identify the optimal coupling condition for a fiber by monitoring the relative power scattered from an engineered defect while moving the fiber in and out of alignment; the result is a heat map of the relative coupling efficiency as a function of fiber position. Light from an optical fiber, positioned with the Nanomax stage was raster scanned across the facet edge of the PIC while the scattered power from an engineered element was monitored further downstream of the waveguide. Simultaneously tracking the fiber displacement from the starting position with the scattered powers generated a heat map of the desired scan area. Results of these scans show a dominant hot spot in the neighborhood of the optimal coupling position due to the correlated relationship between the light scattered and the light in the waveguide. Scans of this nature were performed using a polarization-maintaining (PM) fiber for a SiN-Si and Si-SiN scattering element. Using the polarization response of these scattering elements also allowed for the polarization of the guided mode/s to be evaluated. Placing a linear analyzer at the tube lens of the optical system, input polarization states for TE, TM, and 45 deg were tested for each scattering configuration. In all tests using a linear analyzer for the fiber coupling, the analyzer was orientated to maximize the signal from a TE mode. An additional series of tests were performed on both scattering configurations using a high-NA optical fiber, while SiN WGs were illuminated with 1550 nm. Full-width half-max (FWHM) values for the y and z cross sections of the heat spot, relative powers normalized to the TE mode, and the SNR ratio were computed for all scans. Results of the scans showed consistent results across WG materials, with the polarization response decreasing as states moved away from the TE mode and eventually hit the noise floor when inputting TM modes. Results of scans for a SiN-Si scatterer with a PM fiber are shown in Fig. 6 with Table 2 summarizing the FWHM, relative power, and SNR values for every configuration and input polarization state.[42]

5 Discussion

The engineered scattering elements described here are unique due both to their foundry compatibility and good polarization discrimination. The AIM foundry design rules allow for each scattering element to be designed with subwavelength dimensions as part of the computer aided design. These elements are then part of the photolithography mask used in fabrication and do not require an additional removal step.

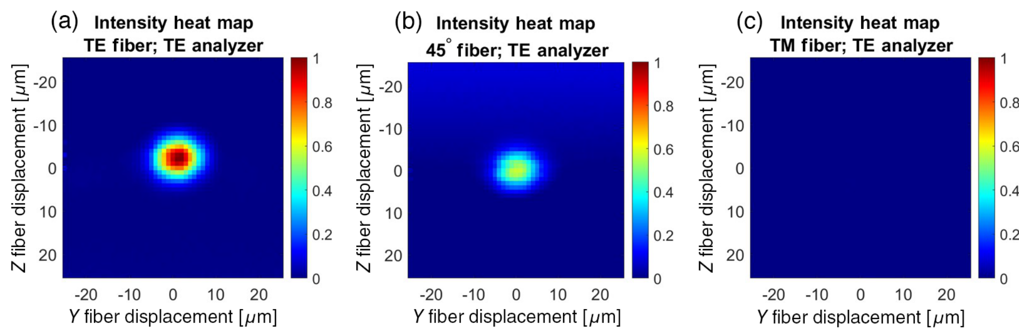

Fig. 6 Heat maps generated from scanning an edge coupled fiber along the PIC facet with a linear analyzer for a SiN-Si scatterer with a PM fiber. Results for input polarization states of: (a) TE, (b) 45 deg, and (c) TM all normalized to the TE scale.

Table 2 Summary of FWHM, relative power compared to TE, and SNR values for different scattering configurations and polarization states tested for fiber edge coupling.

Scattering conf. (fiber)	Polarization state	*Y* FWHM (μm)	*Z* FWHM (μm)	Relative power	SNR
SiN-Si PM fiber	TE	8.6	7.4	1.0	210
	45 deg	9.6	8.8	0.59	72.0
	TM	10	8.2	0.014	1.89
Si-SiN PM fiber	TE	9.6	8.6	1.0	111
	45 deg	8.4	7.9	0.12	50.0
	TM	8.7	7.6	0.019	3.96

Across all designs, engineered scattering elements were identifiable in each PIC when light was coupled into each waveguide. These signals were present regardless of illumination, producing a signal contrast greater than 10× across all designs. The clearly identifiable signal thus allows for quick detection of these elements given *a priori* knowledge of the PIC design and rough placement of the scattering elements.

The polarization response of each scattering element was verified through the developed computational model combining FDTD simulations of the waveguide with numerical vector propagation. The initial design with scattering elements beside the waveguide (i.e., Si-Si) was shown to not display a strong extinction ratio for TE and TM input modes, regardless of feature size or coupling distance. Thus even given the subwavelength nature of the scattering element, observations disproved the preliminary theory that each scattering element would operate as a dipole. Numerical modeling of the design supported this observation, where plotting the polarization ellipse for pixels within the pupil plane of the scattered light for the Si-Si design displayed predominantly left-hand elliptical polarization with a horizontal orientation. Calculated extinction ratios for TE (TM) modes were 1.75 (3.57), supporting the 1.38 (5.87) values captured through the microscope. The elliptical polarization states observed from this source is produced from the complex polarization of evanescent fields in guided modes which require a 3D polarization ellipse to describe their orientation.[43] The projection of the 3D ellipse onto a 2D plane results in the observed elliptical states.[44] Knowledge of the complex nature of the evanescent field led to the next two designs of placing the scattering element above/below the optical waveguide. Based on this orientation, the evanescent fields were more indicative of a transverse dipole.

Simulations of the SiN-Si and Si-SiN designs displayed comparatively higher TE (TM) extinctions of 1509 (256) and 117 (3.70), respectively, and measured extinction values at least 10× greater than the Si-Si designs. While the experimental extinctions for TE (TM) modes were much larger at 73.8 (62.4) for SiN-Si, these results are still far from optimal values. The

extinctions for Si-SiN scatterers were much closer to simulated results with extinction values of 146 (2.71). There are several possible reasons for the low experimental values, including: slight misalignment of the input polarization state[23] and/or the existence of background scatter into the orthogonal polarization state. The latter, in particular, can be more significant for silicon waveguides than for SiN waveguides, offering a possible explanation for the higher extinction in SiN waveguides. Discrepancies between the theory and experiment for the Si-SiN scattering configuration is possibly due to significant diattenuation of SiN waveguides, since a SiN waveguide in an SOI platform having a 3 μm buried oxide layer will tend to experience higher TM loss.

The scope of the scattering elements dimensions and morphology are limited in this paper to provide an initial proof of validity for the elements. Dimensions of the scattering element must follow any foundry's design rules, thus sometimes limiting their size to not provide an accurate approximation of a dipole. Incorporation of multiple scatterers or increasing the area of the scattering element will adjust the polarization state. Designs such as those formerly mentioned have been numerically simulated, but their response is outside the scope of this paper and will be covered in a later design analysis paper. In addition, while each foundry provides different waveguide material thicknesses resulting in different fraction of scattered power, we expect the scattering elements to provide similar polarization responses. As each scattering element couples light from the evanescent field, the resulting polarization state is still dependent on the relative spatial position of the scattering element (i.e., side scatterers observe an elliptical state, while top/bottom are linear).[43]

Fiber bonding to a PIC is a common application within the completed packaging of the fabricated circuit. Ensuring an adequate alignment is a tricky endeavor using precise motor controls, while common methods such as loopbacks and/or taps with power detectors to monitor the degree of coupling. The scattering elements developed in this article have shown a significant contrast with the background scattering and a correlation with the input polarization mode, given the proper scattering configuration. Since the source of the scattering is light within the waveguide, the relative strength of the scattered light is proportional to the efficiency of the light coupled into the guided mode/s. Monitoring the scattered power while tracking the displacement from a starting position has shown a clear hot spot where light is coupling into a guided mode. While all reported scans began with the fiber already aligned, displacing the fiber a random distance but remaining in the scan area still generated a heat spot for optimal coupling. This offers a route to quantitatively assess active alignment without the need for detectors or loop-back connections. Use of this technique is not only limited to physical fiber displacement but can also be utilized with the curing of bonding adhesives which can unknowingly shift the fiber position and lead to a loss of signal in the waveguide. Results of scans such as this provide a basis that can be utilized to discern: (a) the amount of shift needed for the fiber to be properly aligned upon curing, and (b) the relative power lost from the shift in alignment while curing.

While the application of using the engineered scattering elements for alignment of fibers to a PIC has been demonstrated, the absolute power in the waveguide has not been determined. Additional losses from unconsidered defects are mitigated in our analysis due to the scatterers being located hundreds of microns from the input and displaced laterally. This lateral displacement ensures that light scattered from the defect has indeed been coupled to the waveguide. Simulations have shown that the scattering element will typically remove <3.7% of the light in the waveguide with the camera receiving <0.32% of the scattered light. In this way, it is similar to a detector monitoring light coupled through a weak tap, but without the need for a physical probe. Such a scheme measures the optimum position for the fiber, but cannot compensate for, or measure absolutely, light lost from mode adapters, bends, etc. Also, these calculations assume perfectly transmitting optics and an already established guided mode. A more thorough analysis and computation is still on-going, but with suitable measurement, a standardized engineered defect combined with a known microscope system could be calibrated to provide absolute information about the optical power in the guide.

The polarization sensitivity generally matches expected trends based on the waveguide-scatterer configuration. Figure 4 illustrates heat map results for a SiN-Si scattering configuration while varying the input polarization state. As expected, the 45 deg states yields about $1/2$ the power compared with a TE input and a TM input is indistinguishable from the noise floor. This held across all scans regardless of the fiber utilized to input the light. We noted a similar

trend with the Si-SiN configuration with the important difference that a 45 deg input produces a result less than half of the value compared with a TE input. This is likely due to the higher losses of TM modes observed in SiN waveguides, thus any combination of TE+TM modes (e.g., 45 deg or purely TM) will have a reduced power response as less light eventually reaches the scattering element and is detected by the camera.

Guided modes that evanescently couple to a scattering element will scatter a small percentage of the guided light, while also inducing a back-scattered signal in the waveguide. When using scatterers as circuit probes in a PIC, it is therefore important to estimate the excess loss induced by the element as well as the back-scattered component. This is particularly important in applications such as quantum information, where loss becomes a critical factor.[45,46] In simulation we found that each scattering configuration displayed transmission loss <0.05 dB and a back-scattered signal close to the limit of numerical accuracy in the calculation. Specifically, for a TE input, the transmission loss for each configuration is as follows: Si-Si) 0.01 dB, SiN-Si) 0.004 dB, and Si-SiN) 0.05 dB. Back-scattered powers for TE modes were also computed to be: Si-Si) −64.5 dB, SiN-Si) −64.7 dB, and Si-SiN) −36.4 dB. TM inputs displayed results of the same order of magnitude for scattering power and back-scatter.

6 Conclusion

Establishment of national foundries has been a key step toward large-scale production and commercialization of PICs. While acquisition of PICs has risen, testing and improvements of these integrated circuits are still required, especially in monitoring the polarization of light entering and propagating through the circuit. We have simulated and introduced engineered scattering elements to act as optical test points to monitor the polarization of guided light along a waveguide. These elements are polarization dependent, introduce negligible loss into the system, and are foundry compatible. Through the AIM Photonics Foundry, we have tested these scattering elements through three current designs of Si-Si, SiN-Si, and Si-SiN; each displaying a strong signal compared with background light while observed through a SWIR microscope. Two designs additionally showed a strong correlation to the input polarization state, with observed extinction values up to a value of 146. Proper placement of these scattering elements has shown their utility as a metrology tool for measuring relative efficiency in fiber alignment while discriminating the input polarization state. Use of these scattering elements provides a compact and efficient method toward polarization management in PIC technology through individual component testing, polarization conversion, and fiber alignment.

Code, Data, and Material Availability

All data and codes are available in a shareable folder on the "box" cloud storage service. Please contact authors for guidance in retriving the data from the server.

Acknowledgments

Photonic integrated circuits were fabricated through the AIM Photonics foundry, with testing and packaging performed at the AIM Testing and Packaging facility in Rochester, New York. The authors would like to recognize Debra Saulnier for assembly of the SWIR microscope setup and training used for experimental verification. The authors report no conflicts of interest.

References

1. A. Rickman, "The commercialization of silicon photonics," *Nat. Photonics* **8**, 579–582 (2014).
2. L.-W. Luo et al., "WDM-compatible mode-division multiplexing on a silicon chip," *Nat. Commun.* **5**(1), 3069 (2014).
3. G.-H. Duan et al., "10 Gb/s integrated tunable hybrid III–V/Si laser and silicon Mach-Zehnder modulator," in *38th Eur. Conf. and Exhibit. on Opt. Commun.* (2012).
4. Y. A. Vlasov, "Silicon CMOS-integrated nano-photonics for computer and data communications beyond 100g," *IEEE Commun. Mag.* **50**(2), s67–s72 (2012).
5. J. S. Cognetti et al., "Disposable photonics for cost-effective clinical bioassays: application to COVID-19 antibody testing," *Lab Chip* **21**(15), 2913–2921 (2021).

6. S. Arafin and L. A. Coldren, "Advanced INP photonic integrated circuits for communication and sensing," *IEEE J. Sel. Top. Quantum Electron.* **24**(1), 6100612 (2018).
7. A. Gao et al., "Silicon-nanowire-based CMOS-compatible field-effect transistor nanosensors for ultrasensitive electrical detection of nucleic acids," *Nano Lett.* **11**(9), 3974–3978 (2011).
8. A. G. Griffith et al., "Silicon-chip mid-infrared frequency comb generation," in *Conf. Lasers and Electro-Opt. (CLEO) - Laser Sci. to Photonic Appl.* (2014).
9. J. Li et al., "Heterogeneously integrated III–V-on-Si microring resonators: a building block for programmable photonic integrated circuits," null (2021).
10. D. A. B. Miller, D. Miller, and D. A. B. Miller, "Device requirements for optical interconnects to silicon chips," *Proc. IEEE* **97**(7), 1166–1185 (2009).
11. F. Xia, L. Sekaric, and Y. A. Vlasov, "Ultracompact optical buffers on a silicon chip," *Nat. Photonics* **1**(1), 65–71 (2007).
12. C. P. Dietrich et al., "GaAs integrated quantum photonics: towards compact and multi-functional quantum photonic integrated circuits," *Laser Photonics Rev.* **10**(6), 870–894 (2016).
13. J. Carolan et al., "Universal linear optics," *Science* **349**(6249), 711–716 (2015).
14. L. Ranno et al., "Integrated photonics packaging: challenges and opportunities," *ACS Photonics* **9**(11), 3467–3485 (2022).
15. L. Carroll et al., "Photonic packaging: transforming silicon photonic integrated circuits into photonic devices," *Appl. Sci.* **6**(12), 426 (2016).
16. N. Pavarelli et al., "Optical and electronic packaging processes for silicon photonic systems," *J. Lightwave Technol.* **33**(5), 991–997 (2015).
17. T. Matsumoto et al., "Hybrid-integration of SOA on silicon photonics platform based on flip-chip bonding," *J. Lightwave Technol.* **37**(2), 307–313 (2018).
18. I. M. Soganci, A. L. Porta, and B. J. Offrein, "Flip-chip optical couplers with scalable i/o count for silicon photonics," *Opt. Express* **21**, 16075–16085 (2013).
19. T. Barwicz et al., "A novel approach to photonic packaging leveraging existing high-throughput microelectronic facilities," *IEEE J. Sel. Top. Quantum Electron.* **22**(6), 455–466 (2016).
20. J. Nauriyal et al., "Fiber-to-chip fusion splicing for low-loss photonic packaging," *Optica* **6**(5), 549–552 (2019).
21. P. O'Brien et al., *Packaging of Silicon Photonic Devices*, pp. 217–236, Springer Berlin Heidelberg, Berlin, Heidelberg (2016).
22. C. P. Chen et al., "Mode and polarization multiplexing in a Si photonic chip at 40 Gb/s aggregate data bandwidth," *IEEE Photonics Technol. Lett.* **27**(1), 22–25 (2014).
23. A. Singh and A. Singh, "Stokes vector-based polarization management in optical communication system: a review," *Opt. Eng.* **59**(9), 090901 (2020).
24. A. Herrero-Bermello et al., "Design of a broadband polarization splitter based on anisotropy-engineered tilted subwavelength gratings," *IEEE Photonics J.* **11**(3), 6601508 (2019).
25. S. Samanta et al., "A 1 × 2 polarization-independent power splitter using three-coupled silicon rib waveguides," *J. Opt.* **20**(9), 095801 (2018).
26. G. R. Bhatt and B. K. Das, "Improvement of polarization extinction in silicon waveguide devices," *Opt. Commun.* **285**(8), 2067–2070 (2012).
27. W. D. Sacher et al., "Polarization rotator-splitters and controllers in a Si_3N_4-on-SOI integrated photonics platform," *Opt. Express* **22**(9), 11167–11174 (2014).
28. D. Dai et al., "Polarization management for silicon photonic integrated circuits," *Laser Photonics Rev.* **7**(3), 303–328 (2013).
29. T. Komljenovic et al., "Heterogeneous silicon photonic integrated circuits," *J. Lightwave Technol.* **34**(1), 20–35 (2016).
30. J. Chiles et al., "Design, fabrication, and metrology of 10 × 100 multi-planar integrated photonic routing manifolds for neural networks," *APL Photonics* **4**(10), 106101 (2018).
31. X. Chen and H. K. Tsang, "Polarization-independent grating couplers for silicon-on-insulator nanophotonic waveguides," *Opt. Lett.* **36**, 796–798 (2011).
32. J. H. Song et al., "Polarization-independent nonuniform grating couplers on silicon-on-insulator," *Opt. Lett.* **40**, 3941–3944 (2015).
33. N. Ayotte, A. D. Simard, and S. LaRochelle, "Long integrated Bragg gratings for SOI wafer metrology," *IEEE Photonics Technol. Lett.* **27**(7), 755–758 (2015).
34. J. T. Robinson, S. F. Preble, and M. Lipson, "Imaging highly confined modes in sub-micron scale silicon waveguides using transmission-based near-field scanning optical microscopy," *Opt. Express* **14**(22), 10588–10595 (2006).
35. D. Lombardo, I. Agha, and A. Sarangan, "Non-destructive optical loss characterization using designed scattering features," in *Front. Opt.* (2017).

36. N. M. Fahrenkopf et al., "The aim photonics MPW: a highly accessible cutting edge technology for rapid prototyping of photonic integrated circuits," *IEEE J. Sel. Top. Quantum Electron.* **25**(5), 8201406 (2019).
37. J. W. Goodman, *Introduction to Fourier Optics*, W. H. Freeman and Company (2017).
38. L. Mandel and E. Wolf, *Optical Coherence and Quantum Optics*, chapter 3, Cambridge University Press (1995).
39. B. Richards and E. Wolf, "Electromagnetic diffraction in optical systems. II. Structure of the image field in an aplanatic system," *Proc. R. Soc. A Math. Phys. Eng. Sci.* **253**(1274), 358–379 (1959).
40. R. A. Chipman et al., *Polarized Light and Optical Systems*, CRC Press (2018).
41. T. G. Brown, "Chapter 2 - unconventional polarization states: Beam propagation, focusing, and imaging," in *Progress in Optics*, Vol. **56**, Elsevier (2011).
42. I. Z. Sukovaty, T. V. Howard, and T. G. Brown, "Fiber optical coupling with engineered scattering elements," *Proc. SPIE* **12427**, 124270A (2023).
43. A. Aiello and P. Banzer, "The ubiquitous photonic wheel," *J. Opt.* **18**(8), 085605 (2016).
44. G. J. Gbur, *Singular Optics*, CRC Press (2017).
45. F. Flamini, N. Spagnolo, and F. Sciarrino, "Photonic quantum information processing: a review," *Rep. Progr. Phys.* **82**(1), 016001 (2018).
46. J. Wang et al., "Chip-to-chip quantum photonic interconnect by path-polarization interconversion," *Optica* **4**(4), 407–413 (2016).

Tyler V. Howard graduated from Southeast Missouri State University in 2019 with a bachelor's of science in physics and engineering physics: mechanical applications. He joined The Institute of Optics as a PhD student in optics later that same year. He is currently a PhD candidate working on scattering in photonic integrated circuits and microscopy.

Icel Sukovaty graduated with a bachelor's degree in optical engineering from the University of Rochester in 2023. While completing her degree, she pursued research in metrology of photonic integrated circuits (PICs) in Thomas G. Brown's laboratory. She helped develop a method for testing fiber alignment with PICs. She is continuing her research as a master's student planning to graduate in Spring 2024.

Thomas G. Brown is director and professor at the Institute of Optics, University of Rochester. He is a leader in the test assembly and packaging division of AIM Photonics, the editor in chief of the *Journal of Modern Optics*, and co-chair of the annual conference on multidimensional microscopy at Photonics West. He is a Fellow of Optica (formerly OSA) and SPIE and is an honorary member of the Rochester Local Chapter of Optica.